



# Quantification of stored red blood cell fluctuations by time-lapse holographic cell imaging

KEYVAN JAFERZADEH,<sup>1</sup> INKYU MOON,<sup>1,\*</sup> MANON BARDYN,<sup>2</sup> MICHEL PRUDENT,<sup>2</sup> JEAN-DANIEL TISSOT,<sup>2</sup> BENJAMIN RAPPAZ,<sup>3</sup> BAHRAM JAVIDI,<sup>4</sup> GERARDO TURCATTI,<sup>3</sup> AND PIERRE MARQUET<sup>5,6,7</sup>

<sup>1</sup>Department of Robotics Engineering, DGIST, 333 Techno Jungang-daero, Hyeonpung-myeon, Dalseong-gun, Daegu 42988, South Korea

<sup>2</sup>Transfusion Interrégionale CRS, Laboratoire de Recherche sur les Produits Sanguins, Epalinges, Switzerland

<sup>3</sup>Biomolecular Screening Facility, Ecole Polytechnique Fédérale de Lausanne, Lausanne, Switzerland

<sup>4</sup>Department of Electrical and Computer Engineering, U-2157, University of Connecticut, Storrs, CT 06269, USA

<sup>5</sup>Centre de recherche CERVO, 2601 chemin de la Canardière, Québec, QC G1J 2G3, Canada

<sup>6</sup>International Joint Research Unit in Child Psychiatry, Département de Psychiatrie CHUV, Prilly Lausanne, Switzerland, University of Lausanne, Switzerland, Université Laval, Québec, QC G1V 0A6, Canada

<sup>7</sup>Center for Optics, Photonics and Lasers (COPL), Laval University, Quebec City, QC, Canada

\*[inkyu.moon@dgist.ac.kr](mailto:inkyu.moon@dgist.ac.kr)

**Abstract:** We propose methods to quantitatively calculate the fluctuation rate of red blood cells with nanometric axial and millisecond temporal sensitivity at the single-cell level by using time-lapse holographic cell imaging. For this quantitative analysis, cell membrane fluctuations (CMFs) were measured for RBCs stored at different storage times. Measurements were taken over the whole membrane for both the ring and dimple sections separately. The measurements show that healthy RBCs that maintain their discocyte shape become stiffer with storage time. The correlation analysis demonstrates a significant negative correlation between CMFs and the sphericity coefficient, which characterizes the morphological type of erythrocyte. In addition, we show the correlation results between CMFs and other morphological properties such as projected surface area, surface area, mean corpuscular volume, and mean corpuscular hemoglobin.

© 2018 Optical Society of America under the terms of the [OSA Open Access Publishing Agreement](#)

## 1. Introduction

Mature erythrocytes, which are sometimes also referred to as discocytes, are the main cell type in the blood circulation. Their biconcave shape and corresponding deformability are an essential feature of their biological function. Indeed, this configuration, corresponding to the maximum surface area for a given volume, results from their outstanding ability to deform in particular when passing through narrow capillaries during microcirculation. RBCs must adapt to a wide range of capillary sizes, and deform while maintaining their cellular integrity and function. This is made possible by the absence of a three-dimensional (3D) cytoskeleton in RBCs. Their shape and mechanical integrity are maintained instead by a two-dimensional (2D) hexagonal lattice formed of flexible spectrin tetramers, which are linked by actin oligomers. Since the side length of actin (70-80nm) is much smaller than the contour length of a spectrin tetramer (approximately 200nm), it is believed that spectrins are the principal contributors to the bending of membranes or curvature modulus [1–3]. The cell-membrane fluctuations (CMFs) exhibiting by RBCs reflect their outstanding ability to deform [2]. However, the exact mechanisms underlying (CMFs) remain unclear. Mainly, two kinds of processes have been suggested as driving agents of CMFs. The first is the thermal motion,

which is more prominent in membrane regions with a small curvature (the dimple region) [4]. The second is linked to the metabolic activity that determines the adenosine triphosphate (ATP) content in the membrane skeleton and to the involvement of actin. The second type of fluctuations is believed to happen in regions of high curvature, such as the ring section of RBCs [5]. As mentioned earlier, different factors influence the deformability of RBCs. However, under storage conditions (e.g., in blood banks), RBCs undergo molecular, metabolic, biochemical and biomechanical changes, which are commonly referred to as storage lesions. Briefly, such processes result primarily in a decrease in energy metabolism, 2,3-diphosphoglycerate (DPG), ATP, and nitric oxide. Furthermore, during storage, the erythrocyte shape alters from deformable discoid to an irreversibly deformed spherocytocytes. It is due to the irreversible loss of membrane by the formation of micro vesicles, which is the cause of an increased osmotic fragility [6–11]. It is understood that these changes are associated with decreased deformability, poor functionality of RBC and consequently with the removal of RBCs from the bloodstream [12–15]. One important question is regarding the extent to which the RBC biomechanical properties may be altered during the storage time. Considering that CMFs reflect these biomechanical properties, the monitoring of their evolution as a function of storage time could represent an efficient way to address this important question. Specifically, we propose to study the evolution of CMFs within the discocyte RBC subpopulation, i.e. the RBCs having shown the capacity to maintain a biconcave shape over the storage time. Indeed, it has been described that during their transformation into transient echinocytes and finally spherocytes, RBCs exhibit a significant CMF decrease [4, 16]. In addition, when transfused the spherocytes do not recover a healthy discoid shape but are subjected to a phagocytic removal. Practically, discocyte RBC morphological properties including projected surface area (PSA), surface area, sphericity coefficient as well as the two clinically relevant parameters, the mean corpuscular volume (MCV) and the mean corpuscular hemoglobin (MCH), were measured at the single-RBC level. Then, the correlations between these morphological parameters and the CMFs, are calculated at different storage times.

In order to address these questions, we propose automated methods for measuring quantitative fluctuations rate, at the single-RBC level, as a function of their storage time, using time-lapse digital holographic microscopy imaging. We also analyze both the ring and dimple regions of the cell separately, according to the observations mentioned above. Quantitative phase images (QPIs) were acquired every few days over a 71-day period to investigate the alterations of RBC parameters over storage time systematically. The erythrocyte concentrate (EC) from which the RBC samples were collected were prepared at the blood center of the *Transfusion Interrégionale CRS* (Epalinges, Switzerland) as follow:  $450 \pm 50$  mL of whole blood were collected and mixed with 63 mL citrate-phosphate-dextrose (CPD) anticoagulant. The bags were centrifuged to separate blood components. Then, semi-automated pressure applied to distribute the blood fractions into sterile inter-connected blood bags (Fenwal, Lake Zurich, IL, USA). Finally, to remove residual leukocytes the erythrocytes were filtered and 100 mL of saline-adenine-glucose-mannitol (SAGM) additive solution were added. Five mL of each sample were collected using a sampling site every few days during 71 days (the 4 ECs were stored at  $4^{\circ}\text{C}$ ) [16]. To prepare the RBCs, the EC samples were washed two times with NaCl 0.9% (centrifugation at 2000g, during 10min at  $4^{\circ}\text{C}$ ) and resuspended in HEPA 10mM glucose. The RBCs were then seeded in a 96-well plate coated with poly-L-Ornithine for image acquisition.

Our quantitative analysis reveals some interesting points. First, we demonstrate that older discocytes (71 days storage) exhibit a slightly but statistically significant more pronounced stiffness than younger ones (stored for 4 days). Concretely, the fluctuations rate in the dimple is greater than in the ring section in younger RBCs. Furthermore, the MCV, MCH, PSA, and surface area do not change significantly on these time scales. Interestingly, we show that the CMFs of a whole cell (for cells stored for 4 days) show significant negative correlation with

the sphericity coefficient which means that more RBCs have a spherocyte shape, less fluctuations they can exhibit. In contrast, a significant positive correlation between the dimple fluctuations and the sphericity coefficient is also observed.

## 2. Label-free digital holographic imaging

### 2.1 Digital holographic microscopy

Digital holographic microscopy (DHM) is a promising tool for real-time 3D cell imaging owing to its capability for non-invasive visualization and for quantifying transparent biological cells [17–20]. DHM has been utilized in various kinds of cell studies (protozoa, bacteria, plant cells, blood cells, nerve cells, or stem cells) [21–29], and also human red blood cells [30–35], in the absence of labeling. The general layout of off-axis DHM system is outlined in Fig. 1, which is based on Mach-Zender interferometer. The coherent laser source is divided into object and reference beam using beam splitter (See Fig. 1). The object beam illuminates the specimen and creates the object wave front. A microscope objective (MO) collects and magnifies the object wave front, and the object and reference wave fronts are joined by a beam collector to create the hologram. It should be noted that there is a small tilt angle between the object wave front and reference wave to construct “off-axis” holograms. At the end point interferograms are recorded by a CCD camera and the data is transmitted to a PC for the numerical reconstruction.

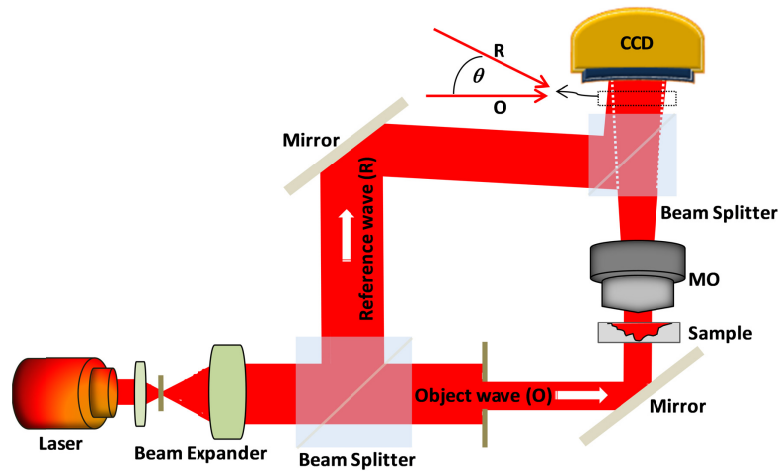


Fig. 1. Schematic of the off-axis DHM setup.

### 2.2 Numerical reconstruction technique

The off-axis holograms between object wave  $O$  and reference wave  $R$  can be expressed as:

$$I_H = |R|^2 + |O|^2 + R^*O + O^*R, \quad (1)$$

where  $R^*$  and  $O^*$  are complex conjugates of the reference and object beams, respectively. The holograms are recorded by the CCD camera (See Fig. 2) to be digitally reconstructed. As it has been mentioned there is a small tilt angle  $\theta$  between  $O$  and  $R$  and it allows us elimination of twin image and zero-order noise. A spatial filter with proper size (Fig. 2(b)) in the Fourier domain (Fig. 2(c)) is designed so the unwanted data can be eliminated by the following:

$$I_H^F = IFFT\{FFT(I_H) \times Filter\} = R^*O \quad (2)$$

where FFT and IFFT respectively are Fourier and inverse Fourier transforms. Since the final image is a phase-contrasted, the hologram should be multiplied by the digital reference wave  $R_D$  during the reconstruction process. This is similar to what happens in classical holography in which the recorded hologram is illuminated by the reference wave. Here, we assume that the reference wave is a perfect plane wave and can be shown by:

$$R_D(k, l) = A_R \exp \left[ i \left( \frac{2\pi}{\lambda} \right) (k_x k \Delta x + k_y l \Delta y) \right], \quad (3)$$

where  $A_R$  is the amplitude,  $\lambda$  is the laser source wavelength,  $\Delta x$  and  $\Delta y$  are the sampling intervals in the hologram plane (pixel size) and  $k_x$  and  $k_y$  are wave vectors which need adjustment to be similar to the experimental reference wave. Another issue is that the MO inserted in the object wave arm introduces phase aberration. This can be numerically resolved by multiplying the reconstructed wave front with the computed complex conjugate of the phase aberration. Eventually the reconstruction of complex amplitude image can be expressed by the Fresnel approximation as following [36]:

$$\Psi(m, n) = A \Phi(m, n) \exp \left[ \frac{i\pi}{\lambda d} (m^2 \Delta \xi^2 + n^2 \Delta \eta^2) \right] \times \text{FFT} \left\{ R_D(k, l) I_H^F(k, l) \times \exp \left[ \frac{i\pi}{\lambda d} (k^2 \Delta x^2 + l^2 \Delta y^2) \right] \right\}_{m, n}, \quad (4)$$

where  $A$  is a constant complex value,  $k, l, m,$  and  $n$  are integers ( $-N/2 \leq k, l, m, n \leq N/2$ ; and  $N \times N$  is the number of pixels in CCD camera  $1024 \times 1024$ ),  $I_H^F$  is the filtered hologram and  $\Phi(m, n)$  is the digital phase mask for the phase aberrations correction calculated by:

$$\Phi(m, n) = \exp \left[ \frac{-i\pi}{\lambda D} (m^2 \Delta \xi^2 + n^2 \Delta \eta^2) \right], \quad (5)$$

Moreover,  $\Delta \xi, \Delta \eta$  are the sampling intervals in the observation plane expressed by:

$$\Delta \xi = \Delta \eta = \frac{\lambda d}{N \Delta x}, \quad (6)$$

where  $d$  denotes distance between camera plane (hologram plane) and image plane. A fine adjustment of  $k_x, k_y$  and  $D$  can be performed in the absence of fringes by removal of residual gradients or curvature of the reconstructed phase distribution in some area of the image where a constant phase is presumed [36].  $D$  is the parameter that must be adjusted to compensate the wave-front curvature according to the distance between MO and specimen, and MO and the image plane evaluated by [36]:

$$\frac{1}{D} = \frac{1}{d_i} \left( 1 + \frac{d_o}{d_i} \right), \quad (7)$$

where  $d_i$  is the distance between MO and image plane and  $d_o$  is the distance between the specimen and MO. Since  $\Psi(m, n)$  is an array of complex numbers, the intensity of amplitude image (Fig. 2(e)) can be obtained by:

$$I(x, y) = \text{Re}[\Psi(m, n)]^2 + \text{Im}[\Psi(m, n)]^2. \quad (8)$$

And the phase image (Fig. 2(f)) can be obtained by the argument of:

$$\phi(x, y) = \tan^{-1} \left\{ \frac{\text{Im}[\Psi(m, n)]}{\text{Re}[\Psi(m, n)]} \right\}. \quad (9)$$

Equation (7) returns values that are limited between  $-\pi$  and  $+\pi$ . For the larger samples phase jumps near  $2\pi$  value might appear. This can be resolved by applying a proper phase unwrapping technique [37]. In the case of RBC, we did not find significant phase jumps (signal is within  $2\pi$  value) only in specific cases, e.g. two RBCs are attached along the optical axis. The special cases are not addressed in this work. We also note that when the RBC sample is in perfect focus, the intensity contrast was very low so that the intensity image was adjusted to be out of focus in order to make the RBCs visible (see Fig. 2(e)).

The clinically relevant results of this work is presented in our previous article [16]. The reconstruction process of QPIs was conducted on line using a standard PC at the rate of several images per seconds. Overall, 200 holograms recorded at 20Hz were reconstructed for each sample. In our configuration, the microscope magnification factor and field of view were  $40 \times / 0.75\text{NA}$  and  $150\mu\text{m}$ , respectively. The  $684.5\text{nm}$  laser source delivered to the specimen plane an intensity of  $\sim 200\mu\text{W}/\text{cm}^2$ , which is nearly six orders of magnitude less than intensities typically associated with confocal fluorescence microscopy. With this amount of light, the required exposure time was only  $0.4\text{ms}$ . Image reconstruction was implemented using C++ and all analyses were carried out using the MATLAB software.

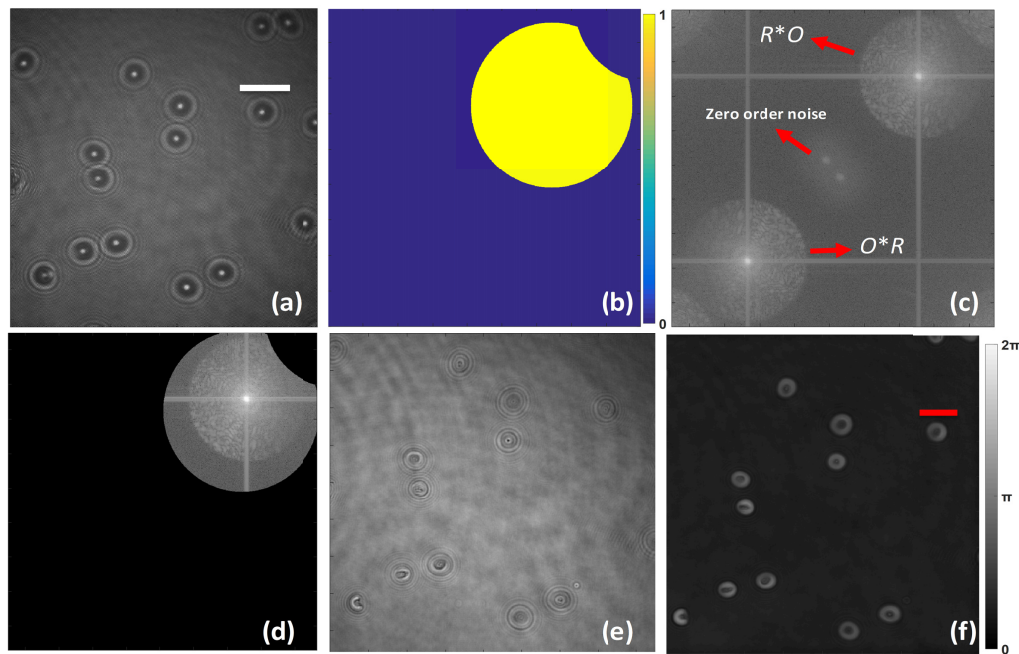


Fig. 2. (a) recorded off-axis hologram (white line is  $500\mu\text{m}$  in CCD plane), (b) filter to remove the twin image and zero-order noise, (c) Fourier transformation of the off-axis hologram, (d) the filtered off-axis hologram in the Fourier domain, (e) amplitude image; the intensity is adjusted for the best visualization, and (f) the contrast phase image after numerical reconstruction (red line is  $10\mu\text{m}$  in the image plane).

### 3. Red blood cell parameters

#### 3.1 Cell thickness

After single-cell QPIs extraction and applying morphological operators, the thickness, at a single cell level can be calculated. The data provided by QPIs in this study are in the form of phase values, from which cell thickness images were obtained:

$$h(x, y) = \frac{\lambda \times \phi(x, y)}{2\pi(n_{RBC} - n_m)}, \quad (10)$$

where  $h(x, y)$  is the RBC thickness, and  $n_{RBC}$  and  $n_m$  are the refractive indices of the RBC and HEPA medium, respectively. The value for  $n_{RBC}$  is previously obtained by the method called decoupling technique [32, 38] and it is reported to be  $1.418 \pm 0.012$  over a spherocyte population. This assumption is valid if the hemoglobin content remains stable in time, we observed within the same EC. The refractive index of HEPA ( $1.3334 \pm 0.0002$ ) is measured at room temperature precisely with Abbe-2WJ refractometer at the wavelength similar to the DHM laser diode.

#### 3.2 Membrane fluctuation rate

Different techniques have been proposed to measure fluctuations in RBC membranes [3–5, 13, 39–46]. However, their separate applications to the ring and dimple sections remain to be carried out, since the sources of their respective fluctuations could be distinct [4]. To calculate the fluctuations rate, we consider the statistical model of Rappaz et al. [5]. Briefly, this requires the definition of a region of interest (ROI) and two independent variables:  $std(h_{cell} + h_{background})$ , the temporal deviation within the RBC area (combining both the cell fluctuations and noise), and  $std(h_{background})$ , the mean temporal deviation calculated over all the pixels located outside the RBC area (see Fig. 3). The measured standard deviations for one pixel outside the cell (Fig. 4 point “A”), on the ring (Fig. 4 point “B”) and at the center (Fig. 4 point “C”), are 17, 42 and 29 nm, respectively, indicating that the membrane fluctuation amplitudes are significantly larger than the background noise level (see Fig. 4 and Visualization 1). Accordingly, the fluctuations at each single pixel CMF( $x, y$ ) can be evaluated as [5].

$$CMF_{cell}(x, y) = \left[ \left( std(h_{cell} + h_{background})(x, y) \right)^2 - \left( std(h_{background}) \right)^2 \right]^{1/2}. \quad (11)$$

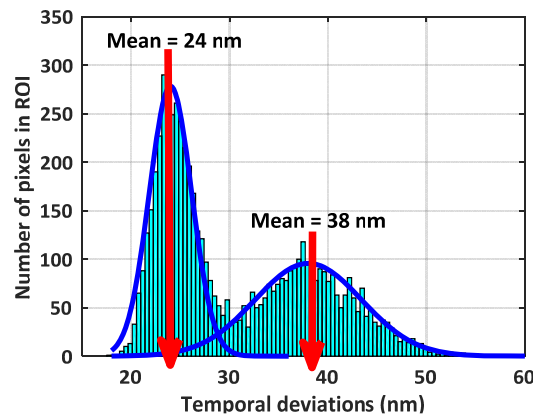


Fig. 3. Distribution of temporal deviations within a ROI; the left-side distribution represents the background and the right side corresponds to the RBC area (cell membrane and noise together).

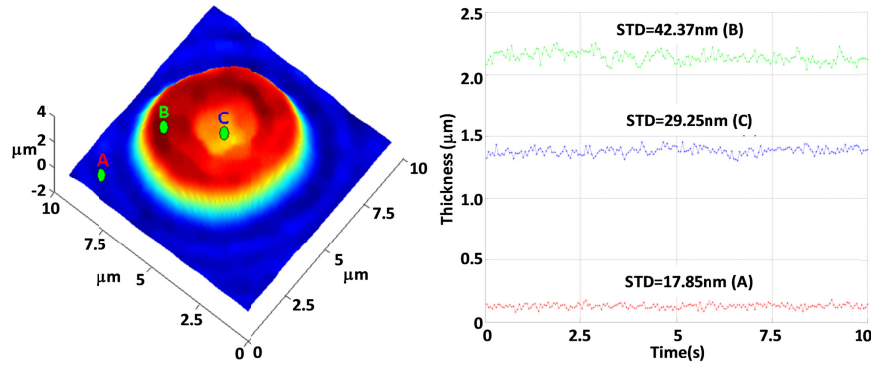


Fig. 4. Thickness signals and STD of changes in three different regions recorded at 20Hz over a 10s period (“A” denotes a background location, “B” is on the cell ring, and “C” is in the dimple region). The standard deviations of the signal are 17, 42, and 29nm, respectively (See Visualization 1).

It should be noted that an RBC occasionally displays significant lateral displacements in time-lapse sequences. The lateral movement of RBCs, could be caused by the loose attachment of the cell to the substrate (only a small portion of the membrane is in contact with the substrate). Such cases also display strong changes in CMFs. We canceled these lateral displacements by utilizing the *ImageJ* [47] software and the *StackReg* [48] plugin. Another concern is the steep membrane gradient at the cell border and around the center of the cell, where a small lateral displacement of the cell membrane has a strong impact on the thickness value, since the thickness is along the  $z$ -axis (blue vector in Fig. 5(b)). In order to avoid systematically overestimating cell fluctuations in such steep-slope regions, cell fluctuations must be evaluated in a direction perpendicular (normal) to the cell membrane (green vectors in Figs. 5(a) and (b)). Finally, normal fluctuations can be estimated as:

$$h_n(x, y) = h(x, y) \times \cos(\theta(x, y)). \quad (12)$$

To calculate  $\theta$ , normal vectors at each vertex of the RBC mesh are measured (see Figs. 5(a)). To do so, a bicubic fit of the data in the  $x$ ,  $y$ , and  $z$  axis are performed and then diagonal vectors are computed and crossed to form the normal at each vertex. Finally,  $\theta$  is measured by:

$$\theta(i, j) = \tan^{-1} \left\{ \frac{N_z(i, j)}{\sqrt{(N_x^2(i, j) + N_y^2(i, j))}} \right\}, \quad (13)$$

where  $N_x(i, j)$ ,  $N_y(i, j)$  and  $N_z(i, j)$  are the normal for pixel  $(i, j)$  in,  $x$ ,  $y$ ,  $z$  directions, respectively.

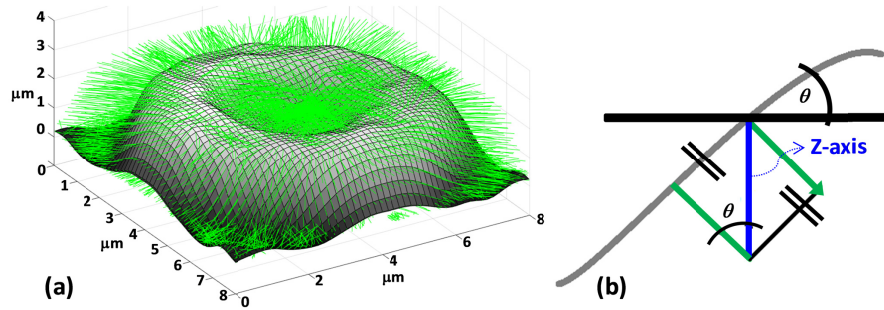


Fig. 5. (a) RBC mesh with normal vectors. (b) X-Z view of the membrane surface and its normal vector.

The deviation map of the cell is obtained by Eq. (11).  $std(h_{cell} + h_{background})(x,y)$  which is the temporal deviation within the ROI combining both the cell fluctuations and noise is measured. Also the average value of  $std(h_{background})$  which is the temporal deviation of all the pixels outside the RBC's projected area is calculated. The two measured values are substituted into the Eq. (11) and the map is evaluated. CMF of the whole cell, dimple and ring is the average of the  $CMF(x,y)$  over the projected area of the whole cell, dimple and ring respectively. We used binary masks to analyze the ring and the dimple sections of RBCs separately, and to isolate the ROI background area. The masks were generated by applying thresholding and a binary operator to implement an “erosion” effect (a few microns erosion). It turns out that the CMF amplitude of the whole membrane, ring, and dimple are  $35 \pm 4.7$  ( $n = 33$ ; RBC age is 4 days)(in agreement with previously reported value [5]),  $35 \pm 5.2$ , and  $36 \pm 5.3$  nm, respectively (see Fig. 6).

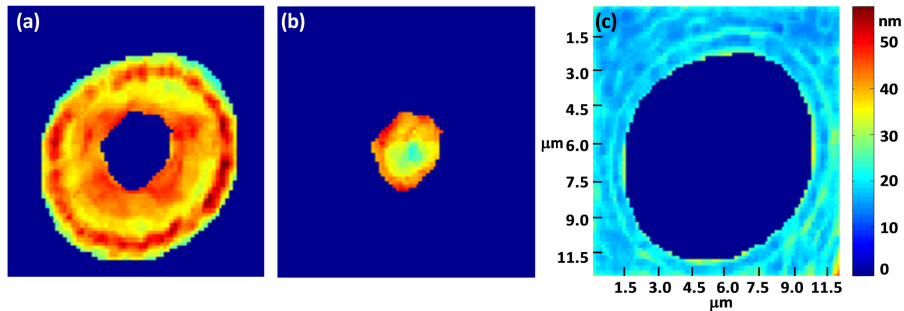


Fig. 6. Deviation map of (a) the ring and (b) dimple sections of a RBC, and (c) the background (after 4 day of storage). Color-bar scale has units of nanometers.

Biconcave and spherocyte morphologies are separated systematically using sphericity coefficients (stomatocytes are removed from the biconcave set). The sphericity coefficient  $k$  is the ratio of the RBC thickness  $h_c$  at the cell center to the thickness  $h_t$  at a radius that is halfway to the cell perimeter [31]:

$$k = \frac{h_c}{h_t}. \quad (14)$$

This metric can distinguish between three types of RBCs. A value of  $k$  less than unity characterizes a biconcave RBC, a value close to 1 denotes a flat-disk biconcave RBC, and a value greater than 1 tends to a spherocyte. In this paper, a threshold value of  $k_t = 0.97$  is assigned to distinguish biconcave cells from spherocytes and echinocytes. After making two masks to isolate the cell and background by applying a proper threshold and several image processing techniques (dilation, erosion, region filling and connecting components), we

calculate the projected surface area (PSA) of the cell. The cell radius can then be evaluated as:

$$r \cong \left( \frac{PSA}{\pi} \right)^{\frac{1}{2}}, \quad (15)$$

where PSA is defined as:

$$PSA = Np^2, \quad (16)$$

where  $N$  is the total number of pixels constituting the RBC projected area resulting from the image segmentation algorithm and  $p$  denotes the pixel size in the phase image ( $0.142\mu\text{m}$ ). Using  $r$ , we can select candidate pixels that are likely to lie near the ring section (blue points in Fig. 7). Since the above procedure cannot precisely identify the points located exactly on the ring section, we search for the pixel with the greatest thickness value near each candidate pixel (within a region of size  $3 \times 3$  pixels). Finally, we define  $h_i$  as the arithmetic average of the heights of all these updated points (red points in Fig. 7). The single green point ( $h_c$ ) is the center of the bounding box of the projected area of RBC on the  $x$ - $y$  plane. After image segmentation and thresholding to binarize the projected area, a rectangle is bounded on the binary result. The center of the bounding box is a quick estimation of the center of the projected area.

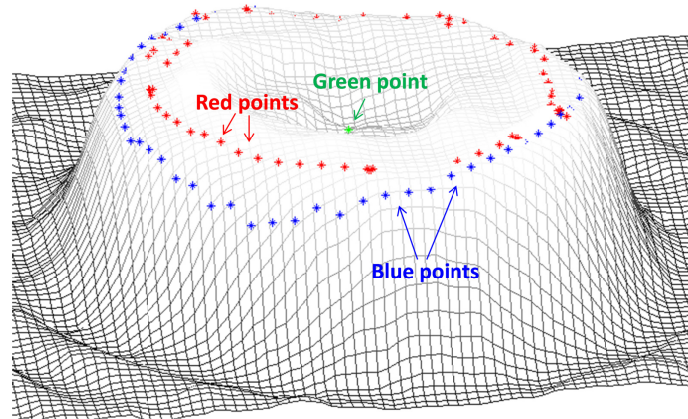


Fig. 7. Blue points show the points obtained by using  $r$ . The red points identify the maximum values within a range of  $3 \times 3$  pixels from the blue points. The green point shows the geometric center of the cell and is obtained by finding the geometrical center of the bounding box on projected area or RBC.

### 3.3 Morphological and hemoglobin related parameters

For the purpose of correlation analysis, this study considers morphological parameters (the mean corpuscular volume (MCV), PSA, surface area and sphericity coefficient) and mean hemoglobin content. The RBC volume at the single-cell level in a DHM thickness image can be expressed as:

$$V \cong p^2 \sum_{(i,j) \in S_p} h(i,j), \quad (17)$$

where  $h(i,j)$  is the thickness value at pixel  $(i,j)$  and  $S_p$  is the RBC's projected area. The thickness summation is achieved over all the pixels  $(i,j)$  of  $S_p$ . In order to measure the surface area, we used the method described in our previous paper [31]. Simply put, the RBC mesh (see Fig. 7) is decomposed into smaller regular triangles, the total sum of which gives the total surface area. Covering the entire surface area of an RBC by small triangles can provide a

high accuracy estimation of the mesh [31]. The surface area of any of these triangles is evaluated by the Heron formula. The total surface area is the surface area of the top view summed with the projected surface area.

The mean corpuscular hemoglobin (MCH) of RBCs can be measured by calculating dry mass of the RBCs since RBCs are mainly composed of hemoglobin [32, 49]:

$$MCH = \frac{10 \phi_{SP} \lambda PSA}{2\pi\alpha_{Hb}}, \quad (18)$$

where  $\phi_{SP}$  is the mean phase value of RBC's projected area, and  $\alpha_{Hb} = 0.00196$  dl/g is a constant known as the specific refraction increment related mainly to the protein concentration.

#### 4. Quantitative analysis of RBC fluctuations

In this paper, numbers written after a  $\pm$  sign denote a standard deviation (STD). In our correlation analysis, we calculated the Pearson product-moment correlation coefficient and adopted a 95% confidence level when applying the  $t$ -test method [50]. Error bars shown in the plots represent twice the corresponding standard deviations.

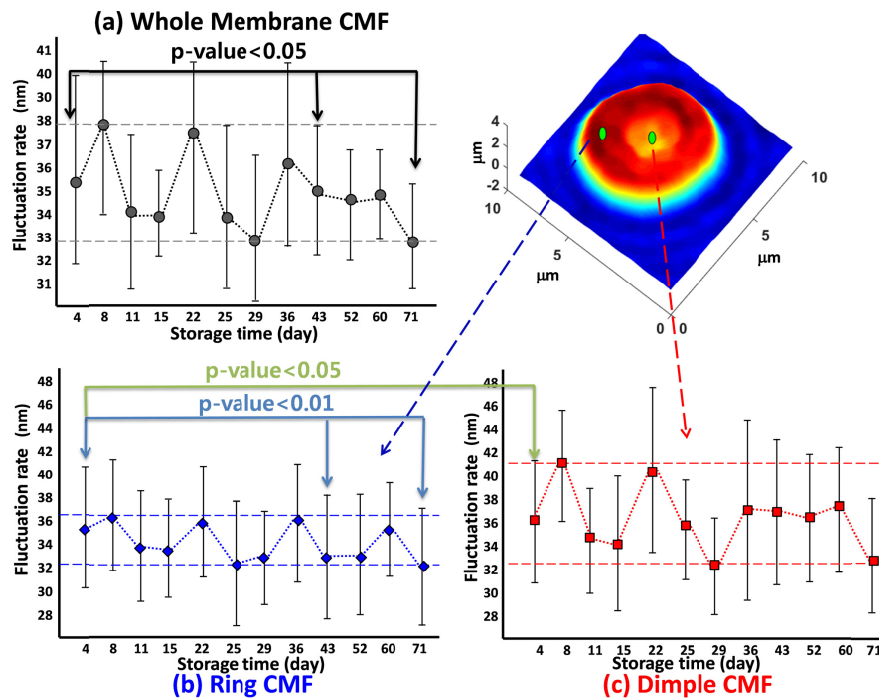


Fig. 8. Evolution of fluctuations amplitude over storage time for (a) the whole membrane, (b) the ring, and (c) the dimple region. The length of the error bars measures two standard deviations (Statistical test is two-sample Kolmogorov-Smirnov test;  $p < 0.05$  is considered as significant).

The impact of storage time was assessed by measuring the time courses of the fluctuations rates, morphological parameters, and the MCH. In this study, more than 32 RBCs were extracted from each image (4 ECs) to measure these different parameters. We also found a small increase in the sphericity coefficient, signifying that the cells are becoming more spherical, less deformable, and stiffer [3, 12, 13, 31], which arguably also affects the fluctuations rate. Concretely, the sphericity coefficient increases from  $0.74 \pm 0.09$  in young

cells (stored for 4 days) to  $0.79 \pm 0.12$  in older cells (stored for 71 days), consistent with reported values [30, 31]. In the case of older RBCs, the STD value of the sphericity coefficient is significantly larger ( $\pm 0.12$ ). We believe that reflects the early phase of the gradual discocyte-spherocyte transformation process. In contrast the MCH does not change over the time of storage and only fluctuates around its average value of  $32 \pm 0.6\text{pg}$  (See Fig. 9), consistent with earlier reports [3, 30, 31, 38]. Moreover, MCH is in agreement with the value obtained by Sysmex KX-21 in the present study (See Fig. 9). This constancy indicates that, while biconcave RBCs undergo morphological changes during storage, they do not leak hemoglobin into the storage solution [3, 13].

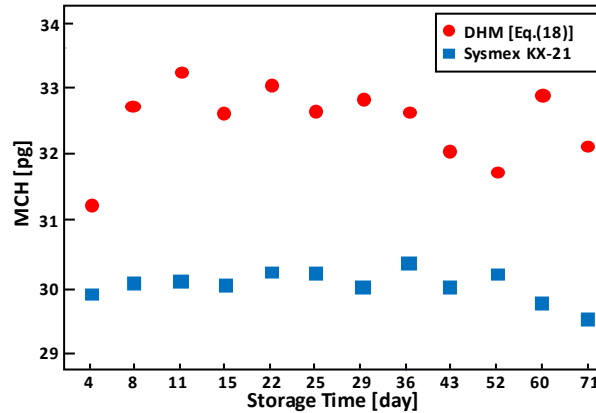


Fig. 9. MCH changes versus storage time. Blue points are MCH obtained by Sysmex KX-21 hematology analyzer and red points are MCH obtained by Eq. (18).

The CMF amplitude fluctuates over the storage time. However, the general trend of the CMF amplitudes as a function of the storage time of the whole RBC, the ring, and the center are to decrease (F-statistics suggest that the linear regression line has a slope that is significantly different from zero;  $p$ -value  $< 0.05$ ), consistent with earlier findings [3]. Our experimental reflecting that RBC membranes stiffen with storage time, in agreement with the reported decrease in deformability [3, 12, 13, 46]. According to Fig. 8, fluctuation amplitude at the dimple are generally larger than in the ring region ( $p < 0.05$ ; two-sample Kolmogorov-Smirnov test), as expected and in agreement with the results of Rappaz et al. [5] (Age of RBC is 4 days).

Figure 10 shows the correlation analyses of the fluctuation amplitudes - the whole RBC membrane and the dimple section - of young RBCs (stored for 4 days;  $n = 33$ ) as functions of the morphological and MCH parameters. The ring section exhibits the same trend as the whole RBC membrane. We therefore decided to exclude ring-section results from our correlation analysis results shown in Fig. 10. Interestingly, the CMF amplitude of the whole RBC exhibits a strong negative correlation with the sphericity coefficient ( $p < 0.05$ ; Pearson product-moment correlation test). The greater  $k$  is the CMF amplitude of the whole RBC is fewer. This can rise from the fact that the more spherical RBCs are, the stiffer they become [12, 46]. On the other hand, there is a significant positive correlation between the CMF amplitude in the dimple region and the  $k$  factor (Fig. 10(a)). The lower the PSA of a RBC, the larger the observed CMF amplitude (Fig. 10(b)). The fluctuation amplitudes of both the whole RBC membrane and dimple region (Fig. 10(c)) have no significant correlation with the MCH, consistent with previous findings [4, 46]. Figure 10(d) and 10(e) shows that CMF amplitudes are not correlated with the MCV and surface area value. We also evaluated the correlation between the CMF amplitudes and  $k$  factor and MCH parameters of RBC for two storage times namely 43 and 71 days (See Fig. 11). Our statistical model for evaluating CMF amplitudes suggests that both the ring and dimple regions differ between young and old

discocyte RBCs. Furthermore, our results about MCH reveal that the hemoglobin content of RBCs remains constant over time. The constancy of the PSA during blood banking shows a tendency of biconcave RBCs to maintain their general structure.

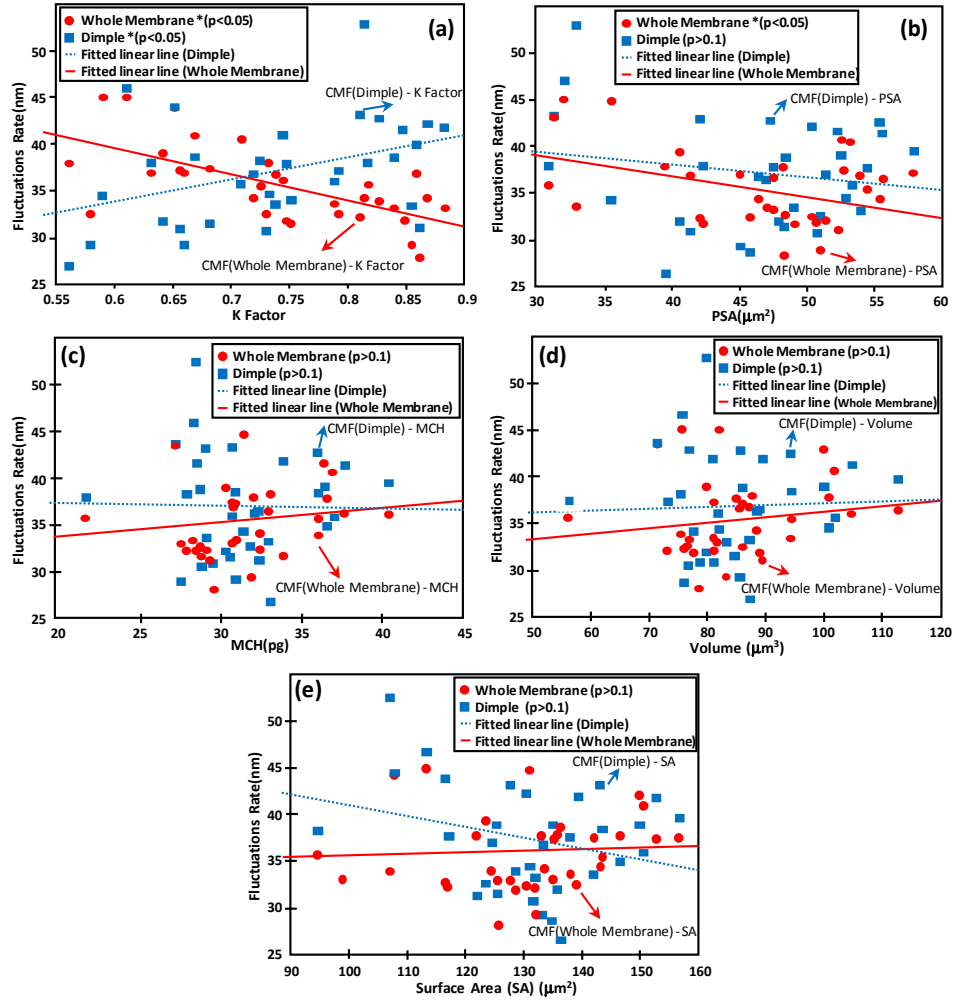


Fig. 10. Correlation measurements between the fluctuation rate and the morphological and hemoglobin parameters, for the entire membrane and the dimple region of discocyte RBCs. (a) sphericity coefficient ( $k$  factor), (b) PSA, (c) MCH, (d) MCV, and (e) surface area. Storage time is 4 days and  $n = 33$ . (An asterisk \* indicates a significant linear correlation by Pearson  $p < 0.05$ ).

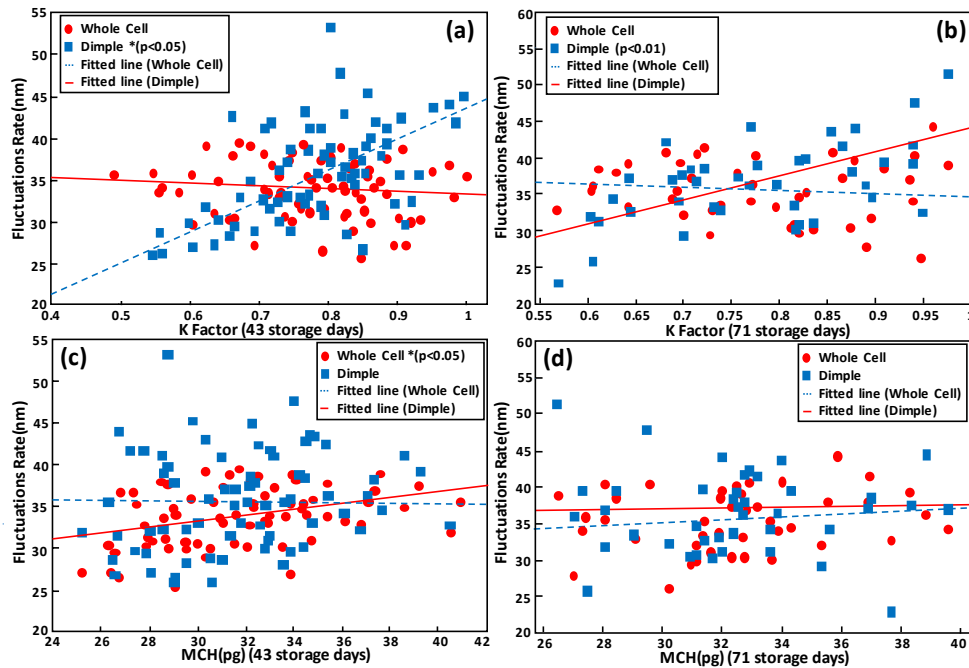


Fig. 11. Correlation analysis between the CMF amplitude and the sphericity coefficient ( $k$  factor) and MCH for the entire membrane and the dimple region of discocyte RBCs for two storage times of 43 days and 71 days. (a) and (b) sphericity coefficient for 43 and 71 days, respectively. (c) and (d) MCH for 43 and 71 days, respectively ( $n = 33$ ; Asterisk \* indicates a significant linear correlation by Pearson  $p < 0.05$ ).

During circulation, normal RBCs must deform to pass through capillaries having a diameter almost half the size of a typical RBC. Their resistance to deformation may not, therefore, be substantial but not too small either, lest it compromise the integrity of the cell in normal circulation [45]. Previous experiments [3, 12, 13, 42] have revealed that RBCs become less deformable and much stiffer over longer storage periods. The consequences of this loss of RBC deformability are significant and potentially seriously detrimental to human organs. It is more difficult, if not impossible, for stiff RBCs to traverse a microcapillary system. Obstructed capillaries cause pain and damage to tissues and organs including infarction and necrosis. Longer transit times through capillaries, resulting from lower RBC deformability, can also hinder oxygen delivery and carbon-dioxide absorption. This increase in stiffness with the aging of the RBC can be explained in several ways. The membrane area is reduced due to the release of microvesicles [51]. Also, ATP is crucial for preserving the biconcave shape, since the depletion of ATP caused a change from the biconcave to the echinocyte shape and finally yielded a spherocyte. This change of shape suggests that ATP and membrane loss stiffen the cytoskeleton and hence constrains the bilayer to a smaller cytoskeleton-projected area. The underlying physical origin of this effect is the change in the number of released spectrin filaments with the reduction in the number of defects as the ATP concentration is reduced [42–44]. Interestingly, it has been shown that the ATP concentration in RBCs decreases with increasing RBC age, or near the end of the RBC lifespan [48]. It is presumed that lower ATP concentrations linked to increasing age should correspond to a denser cytoskeleton, a higher shear modulus, and a drop in fluctuations rate [52]. Figure 12 shows two different discocyte RBCs, imaged after different storage times. Figure 12(a) displays a smaller sphericity coefficient and larger amplitude of fluctuations. In contrast, the older RBCs have a greater sphericity coefficient and a smaller fluctuation amplitude. (See Fig. 12(b)).

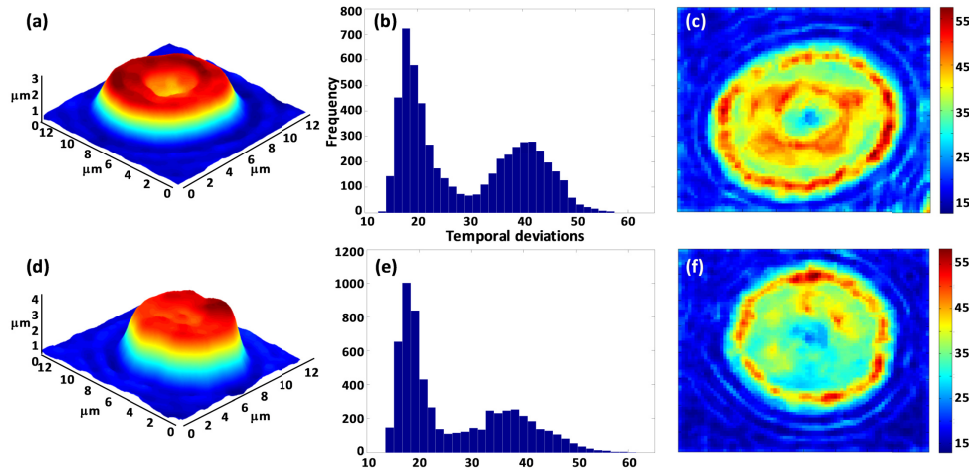


Fig. 12. (a) 3D reconstruction of a RBC (age 4 days) with  $k = 0.85$ , (b) temporal deviation distribution and (c) fluctuation map (average over the whole surface is 34.78nm); (d) 3D reconstruction of a RBC (age 71 days) with  $k = 0.95$ , (e) deviation distribution and (f) fluctuation map (average over the whole surface is 26.33nm). Color-bar scales are in nanometers. See [Visualization 1](#) and [Visualization 2](#) in the supplementary materials.

## 5. Conclusion

In this study, we quantified fluctuations in the discocyte RBC membrane, dimple, and ring in the case of storage lesion using quantitative phase images acquired by DHM. Since DHM is capable of imaging cells at the single-cell level, we evaluated the relationships, as a function of the storage time, between discocyte morphological features and CMFs. Our measurements revealed that membrane fluctuations are significantly correlated with the sphericity coefficient of the monitored discocytes. Concretely, an increase of the discocyte sphericity coefficient is accompanied by a significant decrease of the CMFs - corresponding to the whole RBC, the ring, and the center - translating a loss of deformability.

In contrast, CMFs of young spherocytes (stored for 4 days) corresponding specifically to the dimple region exhibits a positive correlation with the  $k$  factor. So far, we do not have a clear explanation for this observation. Furthermore, an increase of the sphericity coefficient was measured as a function of storage time. Coherently, the general trend of the CMF amplitudes -the whole RBC, the ring, and the center - as a function of the storage time is to decrease stressing that discocytes stiffen as they age.

Taking into account when transfused the discocytes will not be removed in contrast to the spherocytes, we believe that this discocyte deformability study based DHM – a non-invasive label-free technique, compatible with high-content screening capabilities [53] can help to assess the impact of storage duration on blood quality and transfusion outcomes.

## Funding

Basic Science Research Program through the National Research Foundation of Korea (NRF), funded by the Ministry of Science, ICT & Future Planning (NRF-2015K1A1A2029224).

## Disclosures

The authors declare that there are no conflicts of interest related to this article.

## References

1. Z. Tu, "Geometry of membranes," *J. Geom. Symmetry Phys.* **24**, 45–75 (2011).
2. H. Strey, M. Peterson, and E. Sackmann, "Measurement of erythrocyte membrane elasticity by flicker eigenmode decomposition," *Biophys. J.* **69**(2), 478–488 (1995).

3. B. Bhaduri, M. Kandel, C. Brugnara, K. Tangella, and G. Popescu, "Optical assay of erythrocyte function in banked blood," *Sci. Rep.* **4**(1), 6211 (2015).
4. R. Korenstein, S. Tuvia, L. Mittelman, and S. Levin, "Local bending fluctuations of the cell membrane," *Biomechanics of Active Movement and Division of Cells* **84**, 415–423 (1994).
5. B. Rappaz, A. Barbul, A. Hoffmann, D. Boss, R. Korenstein, C. Depeursinge, P. J. Magistretti, and P. Marquet, "Spatial analysis of erythrocyte membrane fluctuations by digital holographic microscopy," *Blood Cells Mol. Dis.* **42**(3), 228–232 (2009).
6. C. Uzoigwe, "The human erythrocyte has developed the biconcave disc shape to optimise the flow properties of the blood in the large vessels," *Med. Hypotheses* **67**(5), 1159–1163 (2006).
7. R. T. Card, "Red cell membrane changes during storage," *Transfus. Med. Rev.* **2**(1), 40–47 (1988).
8. J. Laurie, D. Wyncoll, and C. Harrison, "New versus old blood - the debate continues," *Crit. Care* **14**(2), 130 (2010).
9. A. D'Alessandro, G. Liumbruno, G. Grazzini, and L. Zolla, "Red blood cell storage: the story so far," *Blood Transfus.* **8**(2), 82–88 (2010).
10. D. J. Kor, C. M. Van Buskirk, and O. Gajic, "Red blood cell storage lesion," *Bosn. J. Basic Med. Sci.* **9**(Suppl 1), 21–27 (2009).
11. G. J. Bosman, J. M. Werre, F. L. Willekens, and V. M. Novotný, "Erythrocyte ageing in vivo and in vitro: structural aspects and implications for transfusion," *Transfus. Med.* **18**(6), 335–347 (2008).
12. J. C. Chuitmans, V. Chokkalingam, A. M. Janssen, R. Brock, W. T. Huck, and G. J. Bosman, "Alterations in red blood cell deformability during storage: a microfluidic approach," *BioMed Res. Int.* **2014**, 764268 (2014).
13. H. Park, S. Lee, M. Ji, K. Kim, Y. Son, S. Jang, and Y. Park, "Measuring cell surface area and deformability of individual human red blood cells over blood storage using quantitative phase imaging," *Sci. Rep.* **6**(1), 34257 (2016).
14. I. Safeukui, P. A. Buffet, G. Deplaine, S. Perrot, V. Brousse, A. Ndour, M. Nguyen, O. Mercereau-Puijalon, P. H. David, G. Milon, and N. Mohandas, "Quantitative assessment of sensing and sequestration of spherocytic erythrocytes by the human spleen," *Blood* **120**(2), 424–430 (2012).
15. S. M. Frank, B. Abazyan, M. Ono, C. W. Hogue, D. B. Cohen, D. E. Berkowitz, P. M. Ness, and V. M. Barodka, "Decreased erythrocyte deformability after transfusion and the effects of erythrocyte storage duration," *Anesth. Analg.* **116**(5), 975–981 (2013).
16. M. Bardyn, B. Rappaz, K. Jaferzadeh, D. Crettaz, J. D. Tissot, I. Moon, G. Turcatti, N. Lion, and M. Prudent, "Red blood cells ageing markers: a multi-parametric analysis," *Blood Transfus.* **15**(3), 239–248 (2017).
17. D. Carl, B. Kemper, G. Wernicke, and G. von Bally, "Parameter-optimized digital holographic microscope for high-resolution living-cell analysis," *Appl. Opt.* **43**(36), 6536–6544 (2004).
18. F. Merola, L. Miccio, P. Memmolo, G. Di Caprio, A. Galli, R. Puglisi, D. Balduzzi, G. Coppola, P. Netti, and P. Ferraro, "Digital holography as a method for 3D imaging and estimating the biovolume of motile cells," *Lab Chip* **13**(23), 4512–4516 (2013).
19. I. Moon, M. Daneshpanah, B. Javidi, and A. Stern, "Automated three dimensional identification and tracking of micro/nano biological organisms by computational holographic microscopy," *Proc. IEEE* **97**(6), 990–1010 (2009).
20. B. Javidi, I. Moon, S. Yeom, and E. Carapezza, "Three-dimensional imaging and recognition of microorganism using single-exposure on-line (SEOL) digital holography," *Opt. Express* **13**(12), 4492–4506 (2005).
21. A. Anand, I. Moon, and B. Javidi, "Automated disease identification with 3-D optical imaging: a medical diagnostic tool," *Proc. IEEE* **105**(5), 924–946 (2017).
22. I. Moon and B. Javidi, "3-D visualization and identification of biological microorganisms using partially temporal incoherent light in-line computational holographic imaging," *IEEE Trans. Med. Imaging* **27**(12), 1782–1790 (2008).
23. F. Dubois, C. Yourassowsky, O. Monnom, J. C. Legros, O. Debeir, P. Van Ham, R. Kiss, and C. Decaestecker, "Digital holographic microscopy for the three-dimensional dynamic analysis of in vitro cancer cell migration," *J. Biomed. Opt.* **11**(5), 054032 (2006).
24. K. Alm, H. Cirenajwis, L. Gisselsson, A. Wingren, B. Janicke, A. Molder, S. Oredsson, and J. Persson, *Digital Holography and Cell Studies* (InTech, 2011).
25. B. Rappaz, F. Charrière, C. Depeursinge, P. J. Magistretti, and P. Marquet, "Simultaneous cell morphometry and refractive index measurement with dual-wavelength digital holographic microscopy and dye-enhanced dispersion of perfusion medium," *Opt. Lett.* **33**(7), 744–746 (2008).
26. I. Moon and B. Javidi, "Three-dimensional identification of stem cells by computational holographic imaging," *J. R. Soc. Interface* **4**(13), 305–313 (2007).
27. P. Marquet, B. Rappaz, P. J. Magistretti, E. Cuche, Y. Emery, T. Colomb, and C. Depeursinge, "Digital holographic microscopy: a noninvasive contrast imaging technique allowing quantitative visualization of living cells with subwavelength axial accuracy," *Opt. Lett.* **30**(5), 468–470 (2005).
28. B. Rappaz, E. Cano, T. Colomb, J. Kühn, C. Depeursinge, V. Simanis, P. J. Magistretti, and P. Marquet, "Noninvasive characterization of the fission yeast cell cycle by monitoring dry mass with digital holographic microscopy," *J. Biomed. Opt.* **14**(3), 034049 (2009).
29. B. Rappaz, I. Moon, F. Yi, B. Javidi, P. Marquet, and G. Turcatti, "Automated multi-parameter measurement of cardiomyocytes dynamics with digital holographic microscopy," *Opt. Express* **23**(10), 13333–13347 (2015).

30. I. Moon, F. Yi, Y. H. Lee, B. Javidi, D. Boss, and P. Marquet, "Automated quantitative analysis of 3D morphology and mean corpuscular hemoglobin in human red blood cells stored in different periods," *Opt. Express* **21**(25), 30947–30957 (2013).
31. K. Jaferzadeh and I. Moon, "Quantitative investigation of red blood cell three-dimensional geometric and chemical changes in the storage lesion using digital holographic microscopy," *J. Biomed. Opt.* **20**(11), 111218 (2015).
32. B. Rappaz, A. Barbul, Y. Emery, R. Korenstein, C. Depeursinge, P. J. Magistretti, and P. Marquet, "Comparative study of human erythrocytes by digital holographic microscopy, confocal microscopy, and impedance volume analyzer," *Cytometry A* **73**(10), 895–903 (2008).
33. K. Jaferzadeh and I. Moon, "Human red blood cell recognition enhancement with three-dimensional morphological features obtained by digital holographic imaging," *J. Biomed. Opt.* **21**(12), 126015 (2016).
34. I. Moon, F. Yi, and B. Rappaz, "Automated tracking of temporal displacements of a red blood cell obtained by time-lapse digital holographic microscopy," *Appl. Opt.* **55**(3), A86–A94 (2016).
35. B. Javidi, A. Markman, S. Rawat, T. O'Connor, A. Anand, and B. Andemariam, "Sickle cell disease diagnosis based on spatio-temporal cell dynamics analysis using 3D printed shearing digital holographic microscopy," *Opt. Express* **26**(10), 13614–13627 (2018).
36. E. Cucho, P. Marquet, and C. Depeursinge, "Simultaneous amplitude-contrast and quantitative phase-contrast microscopy by numerical reconstruction of Fresnel off-axis holograms," *Appl. Opt.* **38**(34), 6994–7001 (1999).
37. M. A. Herráez, D. R. Burton, M. J. Lalor, and M. A. Gdeisat, "Fast two-dimensional phase-unwrapping algorithm based on sorting by reliability following a noncontinuous path," *Appl. Opt.* **41**(35), 7437–7444 (2002).
38. B. Rappaz, P. Marquet, E. Cucho, Y. Emery, C. Depeursinge, and P. Magistretti, "Measurement of the integral refractive index and dynamic cell morphometry of living cells with digital holographic microscopy," *Opt. Express* **13**(23), 9361–9373 (2005).
39. F. Brochard and J. Lennon, "Frequency spectrum of flicker phenomenon in erythrocytes," *J. Phys.* **36**(11), 1035–1047 (1975).
40. S. Levin and R. Korenstein, "Membrane fluctuations in erythrocytes are linked to MgATP-dependent dynamic assembly of the membrane skeleton," *Biophys. J.* **60**(3), 733–737 (1991).
41. A. Zilker, H. Engelhardt, and E. Sackmann, "Dynamic reflection interference contrast microscopy - a new method to study surface excitations of cells and to measure membrane bending elastic-moduli," *J. Phys.* **48**(12), 2139–2151 (1987).
42. J. Evans, W. Gratzler, N. Mohandas, K. Parker, and J. Sleep, "Fluctuations of the red blood cell membrane: relation to mechanical properties and lack of ATP dependence," *Biophys. J.* **94**(10), 4134–4144 (2008).
43. N. Gov and S. A. Safran, "Red blood cell shape and fluctuations: cytoskeleton confinement and ATP activity," *J. Biol. Phys.* **31**(3-4), 453–464 (2005).
44. N. S. Gov and S. A. Safran, "Red blood cell membrane fluctuations and shape controlled by ATP-induced cytoskeletal defects," *Biophys. J.* **88**(3), 1859–1874 (2005).
45. G. Marcelli, K. H. Parker, and C. P. Winlove, "Thermal fluctuations of red blood cell membrane via a constant-area particle-dynamics model," *Biophys. J.* **89**(4), 2473–2480 (2005).
46. Y. Kim, H. Shim, K. Kim, H. Park, S. Jang, and Y. Park, "Profiling individual human red blood cells using common-path diffraction optical tomography," *Sci. Rep.* **4**(1), 6659 (2015).
47. C. A. Schneider, W. S. Rasband, and K. W. Eliceiri, "NIH Image to ImageJ: 25 years of image analysis," *Nat. Methods* **9**(7), 671–675 (2012).
48. P. Thévenaz, U. E. Ruttimann, and M. Unser, "A pyramid approach to subpixel registration based on intensity," *IEEE Trans. Image Process.* **7**(1), 27–41 (1998).
49. R. Barer, "Interference microscopy and mass determination," *Nature* **169**(4296), 366–367 (1952).
50. N. Mukhopadhyay, *Probability and Statistical Inference* (CRC Press, 2000)
51. O. Rubin, G. Canellini, J. Delobel, N. Lion, and J. D. Tissot, "Red blood cell microparticles: clinical relevance," *Transfus. Med. Hemother.* **39**(5), 342–347 (2012).
52. M. Prudent, B. Rappaz, R. Hamelin, J. Delobel, M. Mueller, P. Marquet, M. Moniatte, G. Turcatti, J. Tissot, and N. Lion, "Loss of protein TyR-phosphorylation during in vitro storage of human erythrocytes: impact on RBC morphology," *Transfusion* **54**, 49A–50A (2014).
53. J. Kühn, E. Shaffer, J. Mena, B. Breton, J. Parent, B. Rappaz, M. Chambon, Y. Emery, P. Magistretti, C. Depeursinge, P. Marquet, and G. Turcatti, "Label-free cytotoxicity screening assay by digital holographic microscopy," *Assay Drug Dev. Technol.* **11**(2), 101–107 (2013).